Supplemental Material for
"Probing band topology using modulational instability"

Daniel Leykam[1,2], Ekaterina Smolina[3], Aleksandra Maluckov[1,4], Sergej Flach[1,2], and Daria Smirnova[3,5]

[1] *Center for Theoretical Physics of Complex Systems, Institute for Basic Science, Daejeon 34126, Korea*
[2] *Basic Science Program, Korea University of Science and Technology, Daejeon 34113, Korea*
[3] *Institute of Applied Physics, Russian Academy of Science, Nizhny Novgorod 603950, Russia*
[4] *P* Group, Vinča Institute of Nuclear Sciences, University of Belgrade, P.O. Box 522, 11001 Belgrade, Serbia*
[5] *Nonlinear Physics Center, Research School of Physics, Australian National University, Canberra ACT 2601 Australia*

1 Linear Bloch wave spectrum

The linear Hamiltonian of the two-band Chern insulator model considered in the main text is

$$\hat{H}_L(\boldsymbol{k}) = \boldsymbol{d}(\boldsymbol{k})\cdot\hat{\boldsymbol{\sigma}}, \quad d_z = \Delta + 2J_2(\cos k_x - \cos k_y) \quad d_x + id_y = J_1[e^{-i\pi/4}(1+e^{i(k_y-k_x)}) + e^{i\pi/4}(e^{-ik_x}+e^{ik_y})].$$

Its spectrum forms two bulk bands $E_\pm = \pm|\boldsymbol{d}| = \pm\sqrt{d_x^2+d_y^2+d_z^2}$. Explicitly,

$$E_\pm(\boldsymbol{k},\Delta) = \pm\sqrt{4J_1^2\left[1+\cos k_x\cos k_y\right] + \left(\Delta + 2J_2\left(\cos k_x - \cos k_y\right)\right)^2}\,. \tag{S1}$$

The Bloch wave eigenstates $\hat{H}_L(\boldsymbol{k})\,|u_\pm(\boldsymbol{k})\rangle = E_\pm(\boldsymbol{k})\,|u_\pm(\boldsymbol{k})\rangle$ are characterized by a topological invariant, the Chern number [S1]

$$C_\pm = \frac{1}{2\pi}\iint_{BZ}\mathcal{F}_\pm(\boldsymbol{k})\mathrm{d}^2\boldsymbol{k}, \tag{S2}$$

where the integral is computed over the Brillouin zone in the reciprocal space, and

$$\mathcal{F}_\pm(\boldsymbol{k}) = i\left[\langle\partial_{k_x}u_\pm|\partial_{k_y}u_\pm\rangle - \langle\partial_{k_y}u_\pm|\partial_{k_x}u_\pm\rangle\right] \tag{S3}$$

is the Berry curvature. In two band systems the Bloch functions $|u_\pm(\boldsymbol{k})\rangle$ can be expressed as a real unit polarization vector $\hat{\boldsymbol{n}}$ on the surface of the Bloch sphere. To see this, we use the Pauli matrix parameterization of the Bloch Hamiltonian $\hat{H}_L = \boldsymbol{d}(\boldsymbol{k})\cdot\hat{\boldsymbol{\sigma}}$ and multiply the eigenvector equation below Eq. (S1) by $\langle u_\pm(\boldsymbol{k})|$, yielding

$$\boldsymbol{d}\cdot\langle u_\pm|\hat{\boldsymbol{\sigma}}|u_\pm\rangle = E_\pm = \pm|\boldsymbol{d}| \Rightarrow \hat{\boldsymbol{n}}_\pm \equiv \langle u_\pm|\hat{\boldsymbol{\sigma}}|u_\pm\rangle = \pm\boldsymbol{d}/|\boldsymbol{d}|.$$

Moreover, using the $\boldsymbol{d}$ vector parameterization, the Berry curvature takes the simplified form $\mathcal{F}_\pm = \pm\frac{1}{2}\frac{\boldsymbol{d}}{|\boldsymbol{d}|^3}$ [S2]. It follows that the Berry curvature can be written in terms of the polarization vector as

$$\mathcal{F}_\pm(\boldsymbol{k}) = -\frac{1}{2}\hat{\boldsymbol{n}}_\pm\cdot[(\partial_{k_x}\hat{\boldsymbol{n}}_\pm)\times(\partial_{k_y}\hat{\boldsymbol{n}}_\pm)], \tag{S4}$$

with the Chern number counting the number of times $\hat{\boldsymbol{n}}_\pm$ covers the unit sphere [S1]. We note that the interpretation of $C_\pm$ in terms of the wave polarization field can also be generalized to multi-band systems [S3].

The quantized Chern number can only change at topological transitions where the band gap closes. In our two-band Chern insulator model the topological transition occurs when the gap between two bands closes and reopens at $\Delta = \pm 4J_2$. This critical detuning separates phases with zero ($|\Delta| > 4|J_2|$) and nonzero ($|\Delta| < 4|J_2|$) Chern numbers, as depicted in Fig. 1(b) in the main text. The bandgap closure takes place at the high-symmetry points of the Brillouin zone: $\boldsymbol{k}_0 = (\pi, 0)$ [for $\Delta J_2 > 0$, $\Delta = 4J_2$] or $(0,\pi)$ [for $\Delta J_2 < 0$, $\Delta = -4J_2$], where the two bands touch forming a spectral degeneracy, shown in Fig. S1.

2 Linear stability analysis

Here we consider the linear stability of nonlinear Bloch waves in a generic tight binding lattice described by the nonlinear evolution equation

$$i\partial_t\,|\psi(\boldsymbol{r},t)\rangle = (\hat{H}_L + \hat{H}_{NL})\,|\psi(\boldsymbol{r},t)\rangle\,. \tag{S5}$$

We assume that the nonlinear part of the Hamiltonian $\hat{H}_{NL}$ is a diagonal matrix with real elements dependent only on the local on-site intensity, i.e. $\hat{H}_{NL} = \Gamma\mathrm{diag}[f(|\psi_a|^2), f(|\psi_b|^2), ...]$, where f describes the intensity-dependent nonlinear

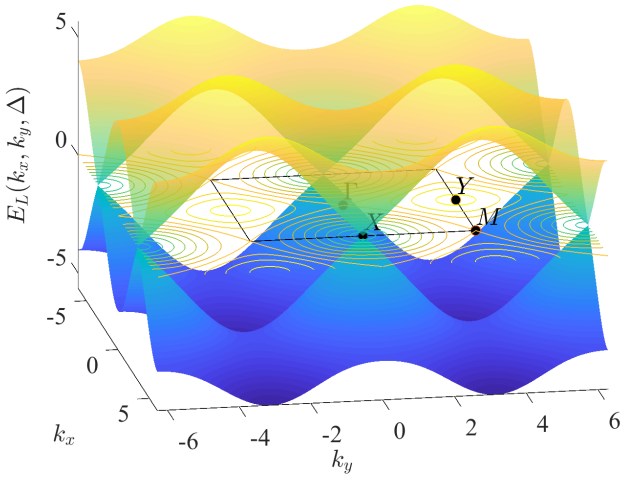

Figure S1: 3D representation of the dispersion $E(k_x, k_y)$ for a square π-flux lattice with parameters $J_1 = 1$, $J_2 = J_1/\sqrt{2}$, $\Delta = 2\sqrt{2}J_1$. Black dots mark the high-symmetry points of the first Brillouin zone traced with a black square.

frequency shift and $a, b, ...$ indexes the sublattice degree of freedom. The linear part of the Hamiltonian $\hat{H}_L$ can be expanded in real space as

$$\hat{H}_L \left|\psi(\boldsymbol{r})\right\rangle = \sum_{\boldsymbol{\delta}} \hat{C}(\boldsymbol{\delta}) \left|\psi(\boldsymbol{r}+\boldsymbol{\delta})\right\rangle, \tag{S6}$$

where summation $\boldsymbol{\delta}$ is over neighbouring unit cells. Transforming to Fourier space, $\left|\psi(\boldsymbol{r})\right\rangle = \sum_{\boldsymbol{k}} \left|\psi(\boldsymbol{k})\right\rangle e^{i\boldsymbol{k}\cdot\boldsymbol{r}}$, we obtain the Bloch Hamiltonian

$$\hat{H}(\boldsymbol{k}) \left|\psi(\boldsymbol{k})\right\rangle = \left(\sum_{\boldsymbol{\delta}} \hat{C}(\boldsymbol{\delta}) e^{i\boldsymbol{k}\cdot\boldsymbol{\delta}}\right) \left|\psi(\boldsymbol{k})\right\rangle. \tag{S7}$$

Note that under the Fourier transform $\hat{H}_L^* \left|\psi(\boldsymbol{r})\right\rangle \to \hat{H}^*(-\boldsymbol{k}) \left|\psi(\boldsymbol{k})\right\rangle$.

To perform the linear stability analysis we consider small perturbations about some nonlinear steady state $\left|\phi(\boldsymbol{r})\right\rangle$ with energy E, i.e. $\left|\psi(\boldsymbol{r},t)\right\rangle = (\left|\phi(\boldsymbol{r})\right\rangle + \left|\delta\phi(\boldsymbol{r},t)\right\rangle)e^{-iEt}$. First, by Taylor expansion of the diagonal nonlinear term and neglecting terms quadratic in the perturbation, we obtain a linearised evolution equation for the perturbation,

$$(i\partial_t + E) \left|p(\boldsymbol{r})\right\rangle = \hat{H}_L \left|p(\boldsymbol{r})\right\rangle + \Gamma \sum_{j=a,b,...} \left[(f(|\phi_j|^2) + f'(|\phi_j|^2)|\phi_j|^2)p_j(\boldsymbol{r}) + f'(|\phi_j|^2)\phi_j^2 p_j^*(\boldsymbol{r})\right] \left|j\right\rangle, \tag{S8}$$

The solution to this set of coupled first order linear differential equations can be expanded in terms of exponential functions as $\left|\delta\phi(\boldsymbol{r},t)\right\rangle = \left|w(\boldsymbol{r})\right\rangle e^{-i\lambda t} + \left|v^*(\boldsymbol{r})\right\rangle e^{i\lambda^* t}$. We collect terms with the same time dependence to obtain the eigenvalue problem

$$\lambda \left|w(\boldsymbol{r})\right\rangle = (\hat{H}_L - E) \left|w(\boldsymbol{r})\right\rangle + \Gamma \sum_{j=a,b,...} \left[(f(|\phi_j|^2) + f'(|\phi_j|^2)|\phi_j|^2)w_j(\boldsymbol{r}) + f'(|\phi_j|^2)\phi_j^2 v_j(\boldsymbol{r})\right] \left|j\right\rangle, \tag{S9}$$

$$\lambda \left|v(\boldsymbol{r})\right\rangle = -(\hat{H}_L^* - E) \left|v(\boldsymbol{r})\right\rangle - \Gamma \sum_{j=a,b,...} \left[(f(|\phi_j|^2) + f'(|\phi_j|^2)|\phi_j|^2)v_j(\boldsymbol{r}) + f'(|\phi_j|^2)\phi_j^{*2} w_j(\boldsymbol{r})\right] \left|j\right\rangle. \tag{S10}$$

Now we assume that steady state is a nonlinear Bloch wave such that $\left|\phi(\boldsymbol{r})\right\rangle = \left|\phi\right\rangle e^{i\boldsymbol{k_0}\cdot\boldsymbol{r}}$. Fourier transforming the above equations, there is coupling between perturbation fields $\left|w(\boldsymbol{k})\right\rangle$ and $\left|v(\boldsymbol{k}-2\boldsymbol{k}_0)\right\rangle$. We obtain the coupled equations

$$\lambda \left|w(\boldsymbol{k}+\boldsymbol{k}_0)\right\rangle = (\hat{H}(\boldsymbol{k}_0+\boldsymbol{k}) - E) \left|w\right\rangle + \Gamma \sum_{j=a,b,...} \left[(f(|\phi_j|^2) + f'(|\phi_j|^2)|\phi_j|^2])w_j + f'(|\phi_j|^2)\phi_j^2 v_j\right] \left|j\right\rangle, \tag{S11}$$

$$\lambda \left|v(\boldsymbol{k}-\boldsymbol{k}_0)\right\rangle = -(\hat{H}^*(\boldsymbol{k}_0-\boldsymbol{k}) - E) \left|v\right\rangle - \Gamma \sum_{j=a,b,..} \left[(f(|\phi_j|^2) + f'(|\phi_j|^2)|\phi_j|^2])w_j + f'(|\phi_j|^2)\phi_j^{*2} w_j\right] \left|j\right\rangle. \tag{S12}$$

This eigenvalue problem has a built-in particle hole symmetry: eigenvalues λ must occur in complex conjugate pairs. Real λ correspond to stable perturbation modes, purely imaginary λ result in exponential instabilities, and complex λ correspond to oscillatory instabilities.

It is instructive to first consider the limit of weak nonlinearity $\Gamma \ll 1$. In this case, we can treat the terms arising due to the nonlinearity as a weak perturbation, $\lambda = \lambda_0 + \Gamma\lambda_1$. The unperturbed eigenvalue problem is

$$\lambda_0 \begin{pmatrix} |w\rangle \\ |v\rangle \end{pmatrix} = \begin{pmatrix} \hat{H}(\boldsymbol{k}_0+\boldsymbol{k}) - E & 0 \\ 0 & -\hat{H}^*(\boldsymbol{k}_0-\boldsymbol{k}) + E \end{pmatrix} \begin{pmatrix} |w\rangle \\ |v\rangle \end{pmatrix}. \tag{S13}$$

The eigenvalues are $\lambda_0 = E_n(\boldsymbol{k}_0+\boldsymbol{k}) - E, -E_n(\boldsymbol{k}_0+\boldsymbol{k}) + E$, with Bloch wave eigenvectors $(|u_n(\boldsymbol{k}_0+\boldsymbol{k})\rangle, 0)^T$, $(0, |u_n^*(\boldsymbol{k}_0-\boldsymbol{k})\rangle)^T$, respectively. Assuming non-degenerate eigenvalues, the first order corrections due to the terms arising from the nonlinearity are

$$\lambda_1 = \sum_{j=a,b,\ldots} [f(|\phi_j|^2) + f'(|\phi_j|^2)|\phi_j|^2]|\langle u_n(\boldsymbol{k}_0 \pm \boldsymbol{k})|j\rangle|^2 = g_{\text{eff}}. \tag{S14}$$

Thus, in this perturbative limit the perturbation modes maintain the same polarization as the lattice's Bloch waves, and their energy shifts are proportional to the squared overlap between linear Bloch waves and the nonlinear stationary state, which justifies the arguments used in the main text.

In two band tight binding models the Bloch Hamiltonian can be parameterized using the Pauli matrices as $\hat{H}(k) = \boldsymbol{d}(k)\cdot\hat{\boldsymbol{\sigma}}$, where $\boldsymbol{d}(k)$ is a real 3 component vector. We obtain the explicit matrix form of the linear stability equations,

$$\lambda \begin{pmatrix} |w\rangle \\ |v\rangle \end{pmatrix} = \begin{pmatrix} \boldsymbol{d}(\boldsymbol{k}_0+\boldsymbol{k})\cdot\hat{\boldsymbol{\sigma}} - E + \Gamma\sum_j (f_j + f_j'|\phi_j|^2)|j\rangle\langle j| & \Gamma\sum_j f_j'\phi_j^2 |j\rangle\langle j| \\ -\Gamma\sum_j f_j'\phi_j^{*2}|j\rangle\langle j| & -\boldsymbol{d}(\boldsymbol{k}_0-\boldsymbol{k})\cdot\hat{\boldsymbol{\sigma}}^* + E - \Gamma\sum_j (f_j + f_j'|\phi_j|^2)|j\rangle\langle j| \end{pmatrix} \begin{pmatrix} |w\rangle \\ |v\rangle \end{pmatrix}, \tag{S15}$$

where $f_j = f(|\phi_j|^2)$ and $f_j' = f'(|\phi_j|^2)$.

For the case of a nonlinear Bloch wave with intensity I_0 localized to the a sublattice analyzed in the main text, we have $|\phi\rangle = (\sqrt{I_0}, 0)$, $d_{x,y}(\boldsymbol{k}_0) = 0$, $d_z(\boldsymbol{k}_0) = \Delta - 4J_2$, and $E = d_z(\boldsymbol{k}_0) + \Gamma f(I_0)$, and the $\boldsymbol{k} = 0$ eigenvalue problem takes the particularly simple form

$$\lambda \begin{pmatrix} w_a \\ w_b \\ v_a \\ v_b \end{pmatrix} = \begin{pmatrix} \Gamma f' I_0 & 0 & \Gamma f' I_0 & 0 \\ 0 & -2d_z(\boldsymbol{k}_0) - \Gamma f & 0 & 0 \\ -\Gamma f' I_0 & 0 & -\Gamma f' I_0 & 0 \\ 0 & 0 & 0 & 2d_z(\boldsymbol{k}_0) + \Gamma f \end{pmatrix} \begin{pmatrix} w_a \\ w_b \\ v_a \\ v_b \end{pmatrix}, \tag{S16}$$

yielding $\lambda = 0, 0, \pm[2d_z(\boldsymbol{k}_0) + \Gamma f(I_0)]$ and a fourfold degeneracy when $\Gamma f(I_0)/2 = -d_z(\boldsymbol{k}_0)$, i.e. when the nonlinear energy shift on the a sublattice is sufficient to close the band gap. Complex instability eigenvalues emerge beyond this threshold intensity.

The threshold intensity is independent of $f'(I_0)$, i.e. the precise form of the nonlinear response function. For example, Fig. S2 shows the dependence of the maximal growth rate on $\Gamma f(I_0)$ and the ratio $r = I_0 f'(I_0)/f(I_0)$. The former describes the nonlinearity-induced change to the sublattice depths, while the latter describes the relative strength of nonlinearity-induced mixing between different perturbation wavevectors. r interpolates between a completely saturated nonlinearity ($r = 0$, corresponding to effectively linear propagation dynamics), and pure Kerr nonlinearity ($r = 1$). We observe that tuning r does not affect the position of the critical stable line, and merely rescales instability growth rate. Thus, the linear stability eigenvalue spectra for the pure Kerr and saturable cases are qualitatively similar, exhibiting the same re-emergence of stability.

3 Nonlinear Dirac model

In this section we examine the dispersion and linear stability of the nonlinear Bloch waves in the vicinity of the high-symmetry point with in-plane wave vector $\boldsymbol{k}_0 = (\pi, 0)$, which can be described by an effective continuum model. In the vicinity of $\boldsymbol{k}_0$, $\boldsymbol{k} = \boldsymbol{k}_0 + \boldsymbol{p}$, the series expansion in the Bloch Hamiltonian $\hat{H}_L(\boldsymbol{k})$ for $|\boldsymbol{p}| \ll 1$ leads to the Dirac-like Hamiltonian

$$\hat{H}_D(\boldsymbol{k}_0 = (0,\pi)) = -J_1\sqrt{2}\,(-p_x\hat{\sigma}_x + p_y\hat{\sigma}_y) + \left(\Delta - 4J_2 + J_2\left[p_x^2 + p_y^2\right]\right)\hat{\sigma}_z\,, \tag{S17a}$$

$$\hat{H}_D(\boldsymbol{k}_0 = (\pi,0)) = -J_1\sqrt{2}\,(-p_x\hat{\sigma}_y + p_y\hat{\sigma}_x) + \left(\Delta - 4J_2 + J_2\left[p_x^2 + p_y^2\right]\right)\hat{\sigma}_z. \tag{S17b}$$

The corresponding evolution equations including the local Kerr nonlinearity $f(I) = I$ can be formulated in the real space in terms of spatial derivatives by substituting $p_{x,y} = -i\partial_{x,y}$ into Eq. (S17b):

$$i\partial_t\boldsymbol{\psi} = \begin{pmatrix} \Delta - 4J_2 - J_2\left[\partial_x^2 + \partial_y^2\right] + \Gamma|\psi_1^2| & J_1\sqrt{2}\,(i\partial_y - \partial_x) \\ J_1\sqrt{2}\,(i\partial_y + \partial_x) & -\Delta + 4J_2 + J_2\left[\partial_x^2 + \partial_y^2\right] + \Gamma|\psi_2^2| \end{pmatrix}\boldsymbol{\psi}. \tag{S18}$$

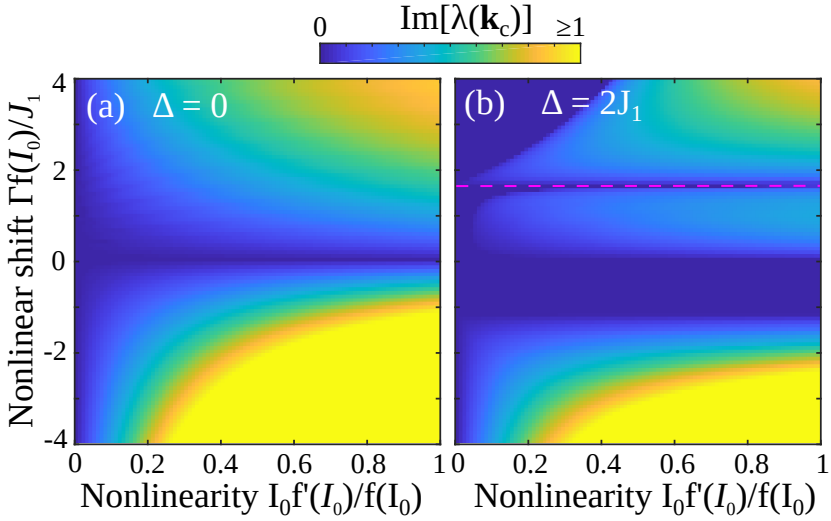

Figure S2: Growth rate of the most unstable perturbation wavevector $\boldsymbol{k}_c$ as a function of the nonlinear frequency shift $\Gamma f(I_0)$ and the relative nonlinear wave mixing strength $I_0 f'(I_0)/f(I_0)$, for the $\Delta = 0$ (a) and $\Delta = 2J_1$ (b) lattices. Purple dashed line in (b) marks the nonlinearity-induced gap closure at $\boldsymbol{k} = \boldsymbol{k}_0$, which is only sensitive to the nonlinear frequency shift.

3.1 Nonlinear dispersion of bulk modes

We search for the solution of (S18) in the form of weakly nonlinear Bloch waves:

$$\begin{pmatrix} \psi_1 \\ \psi_2 \end{pmatrix} = \begin{pmatrix} A \\ B \end{pmatrix} e^{-iEt+ip_x x+ip_y y}. \tag{S19}$$

Plugging the spinor (S19) into Eq.(S18) results in the system of equations for the amplitudes A and B

$$\begin{cases} (-E + \Delta - 4J_2 + J_2\left[p_x^2 + p_y^2\right] + \Gamma|A^2|)A - J_1\sqrt{2}\,(p_y + ip_x)\,B = 0\,, \\ (E + \Delta - 4J_2 + J_2\left[p_x^2 + p_y^2\right] - \Gamma|B^2|)B + J_1\sqrt{2}\,(p_y - ip_x)\,A = 0\,, \end{cases} \tag{S20}$$

where the wave vector $\boldsymbol{p} = (p_x, p_y) = p(\cos\theta, \sin\theta)$ can be defined in the polar coordinate system, $p_y + ip_x = ipe^{-i\theta}$.

Denoting the total wave intensity $|A|^2 + |B|^2 = I_0$, we first find the solutions for the lower and upper bands at the zero wave vector $\boldsymbol{p} = 0$:

$$A^{(0)} = 0, \quad |B^{(0)}|^2 = I_0, \quad E_2^{(0)} = -\Delta + 4J_2 + \Gamma|B^{(0)}|^2 = -\Delta + 4J_2 + \Gamma I_0, \tag{S21}$$

$$B^{(0)} = 0, \quad |A^{(0)}|^2 = I_0, \quad E_1^{(0)} = \Delta - 4J_2 + \Gamma|A^{(0)}|^2 = \Delta - 4J_2 + \Gamma I_0. \tag{S22}$$

At the intensities above the critical value $I_0 \geq \pm 2\frac{(\Delta - 4J_2)}{\Gamma}$, we get the additional doubly degenerate solution

$$|A^{(0)}|^2 = \frac{I_0}{2} - \frac{\Delta - 4J_2}{\Gamma}, \quad |B^{(0)}|^2 = \frac{I_0}{2} + \frac{\Delta - 4J_2}{\Gamma}, \quad E_3^{(0)} = \frac{\Gamma I_0}{2} \tag{S23}$$

with the eigenvectors:

$$\begin{pmatrix} A^{(0)} \\ B^{(0)} \end{pmatrix} = \frac{1}{\sqrt{2}} \begin{pmatrix} e^{i\varphi}\sqrt{I_0 - \dfrac{2\,(\Delta - 4J_2)}{\Gamma}} \\ \pm\sqrt{I_0 + \dfrac{2\,(\Delta - 4J_2)}{\Gamma}} \end{pmatrix}, \tag{S24}$$

where φ is an arbitrary phase depending on which direction we approach the degeneracy point $\boldsymbol{p} = 0$. Specifically, this phase uncertainty is lifted if we consider the limit transition to the point $\boldsymbol{p} = 0$ along different directions $\boldsymbol{p}_0(p_0 \to 0) = (p_{0x}, p_{0y}) = p_0(\cos\theta_0, \sin\theta_0)$. According to (S20), the phase shift in spinor (S24) is given by $\varphi = \pi/2 - \arctan(p_{0y}/p_{0x}) = \pi/2 - \theta_0$.

To find the dispersion in the neighborhood of the point $p_x = p_y = 0$, we employ the perturbation theory. Treating p_x and p_y as small perturbations, we expand all quantities to the first order $E = E^{(0)} + E^{(1)} + ...$; $A = A^{(0)} + A^{(1)} + ...$; $B = B^{(0)} + B^{(1)} + ...$ We obtain a cross-like solution describing the nonlinear Dirac cone:

$$E = E_3^{(0)} + E^{(1)} = \frac{\Gamma I_0}{2} \pm \frac{\sqrt{2}J_1\sqrt{p_x^2 + p_y^2}}{\sqrt{1 - \frac{4(\Delta - 4J_2)^2}{I_0^2\Gamma^2}}}. \tag{S25}$$

Thus, at $\Gamma^2 I_0^2 > 4\left(\Delta - 4J_2\right)^2$ one of the dispersion curves develops a loop.

The intensities of two components nearby the cross point are corrected as follows

$$|A|^2 = \frac{I_0}{2} - \frac{\Delta - 4J_2}{\Gamma}\left(1 \mp \frac{2\sqrt{2}J_1\sqrt{p_x^2+p_y^2}}{\sqrt{I_0^2\Gamma^2 - 4(\Delta-4J_2)^2}}\right),\ |B|^2 = \frac{I_0}{2} + \frac{\Delta - 4J_2}{\Gamma}\left(1 \mp \frac{2\sqrt{2}J_1\sqrt{p_x^2+p_y^2}}{\sqrt{I_0^2\Gamma^2 - 4(\Delta-4J_2)^2}}\right). \quad \text{(S26)}$$

Substituting amplitudes (S26) and energy (S25) into the system (S20), we may introduce the local effective Hamiltonian as:

$$\begin{pmatrix} \pm 2\sqrt{2}J_1 \frac{(\Delta-4J_2)\sqrt{p_x^2+p_y^2}}{\sqrt{I_0^2\Gamma^2-4(\Delta-4J_2)^2}} & -\sqrt{2}J_1(p_y+ip_x) \\ -\sqrt{2}J_1(p_y-ip_x) & \mp 2\sqrt{2}J_1 \frac{(\Delta-4J_2)\sqrt{p_x^2+p_y^2}}{\sqrt{I_0^2\Gamma^2-4(\Delta-4J_2)^2}} \end{pmatrix} \begin{pmatrix}\psi_1\\ \psi_2\end{pmatrix} = E^{(1)}\begin{pmatrix}\psi_1\\ \psi_2\end{pmatrix} = \pm\frac{\sqrt{2}J_1\sqrt{p_x^2+p_y^2}}{\sqrt{1-\frac{4(\Delta-4J_2)^2}{I_0^2\Gamma^2}}}\begin{pmatrix}\psi_1\\ \psi_2\end{pmatrix}. \quad \text{(S27)}$$

Next, we derive the exact implicit expression for the nonlinear dispersion $E(p_x, p_y)$. To simplify our derivations, we set $p_x = 0$ and rewrite the system in the form:

$$\begin{pmatrix} E_n - M_n & J_1\sqrt{2}p_y \\ J_1\sqrt{2}p_y & E_n + M_n \end{pmatrix}\begin{pmatrix}A\\ B\end{pmatrix} = 0\,, \quad \text{(S28)}$$

denoting $E_n = E - \Gamma I_0/2$, $M_n = \Delta - 4J_2 + \dfrac{\Gamma I_0\left(\Delta - 4J_2 + J_2 p_y^2\right)}{2(E - \Gamma I_0)} + J_2 p_y^2$. The nonlinear dispersion is then given by

$$E_n^2 = 2J_1^2 p_y^2 + M_n^2(p_y^2). \quad \text{(S29)}$$

The eigenvectors' intensities on the two sublattices satisfy

$$|A|^2 = \frac{I_0}{2} + \frac{(\Delta - 4J_2)\, I_0}{2(-\Gamma I_0 + E)} + \frac{J_2 p_y^2 I_0}{2(-\Gamma I_0 + E)}, \quad \text{(S30)}$$

$$|B|^2 = \frac{I_0}{2} - \frac{(\Delta - 4J_2)\, I_0}{2(-\Gamma I_0 + E)} - \frac{J_2 p_y^2 I_0}{2(-\Gamma I_0 + E)}. \quad \text{(S31)}$$

The implicit relation (S29) can be posed as

$$\left((E - \Gamma I_0/2)^2 - 2J_1^2 p_y^2\right)(E - \Gamma I_0)^2 = \left(\Delta - 4J_2 + J_2 p_y^2\right)^2\left(E - \frac{\Gamma I_0}{2}\right)^2. \quad \text{(S32)}$$

Note, this dispersion relation supports the existence of 2 more loops in addition to the loop at the point $p_y = p_{\rm I} = 0$, described above. This bifurcation occurs at $d_z(\boldsymbol{p}) = 0$:

$$p_y = \pm p_{\rm II} = \pm\sqrt{\frac{4J_2 - \Delta}{J_2}}, \quad \text{(S33)}$$

in the nontrivial phase only, $|\Delta| < 4J_2$. The energies at the points $p_y = \pm p_{\rm II}$ are:

$$E_3^{(0){\rm II}} = \Gamma I_0, \quad \text{(S34)}$$

$$E_{2,1}^{(0){\rm II}} = \Gamma I_0/2 \pm \sqrt{\frac{2J_1^2(4J_2 - \Delta)}{J_2}}. \quad \text{(S35)}$$

Specifically, the energy $E_3^{(0){\rm II}}$ corresponds to two additional cross points, which appear only in the nontrivial case with the eigenvectors

$$\begin{pmatrix} A^{(0){\rm II}} \\ B^{(0){\rm II}} \end{pmatrix} = \begin{pmatrix} e^{i\varphi}\sqrt{\dfrac{I_0}{2} + \sqrt{\dfrac{I_0^2}{4} - 2J_1^2(p_y^{\rm II})^2/\Gamma^2}} \\ \pm\sqrt{\dfrac{I_0}{2} - \sqrt{\dfrac{I_0^2}{4} - 2J_1^2(p_y^{\rm II})^2/\Gamma^2}} \end{pmatrix}. \quad \text{(S36)}$$

The additional crosses appear at the intensities higher $\Gamma I_0/2 = \pm\sqrt{\dfrac{2J_1^2(4J_2 - \Delta)}{J_2}}$ (the sign is chosen depending on sign of the nonlinearity Γ), which is defined by the degeneracy of the cross point and one of the bands at $p_y = \pm p_{\rm II}$.

3.2 Modulation instability

To examine linear stability of the nonlinear Bloch modes, we introduce small complex-valued perturbations to the amplitudes: $A = A_0 + \delta a$, $B = B_0 + \delta b$ and look for the solution in the form:

$$\begin{pmatrix} \psi_1 \\ \psi_2 \end{pmatrix} = \begin{pmatrix} A_0 + \delta a \\ B_0 + \delta b \end{pmatrix} e^{-iEt + ip_x x + ip_y y}. \tag{S37}$$

The equations for deviations $\delta a,\ \delta b$ can be recast as

$$i\frac{\partial}{\partial t}\begin{pmatrix} \delta a \\ \delta b \\ \delta a^* \\ \delta b^* \end{pmatrix} = \hat{L}\begin{pmatrix} \delta a \\ \delta b \\ \delta a^* \\ \delta b^* \end{pmatrix}, \tag{S38}$$

where operator $\hat{L}$ is the 4×4 matrix

$$\hat{L} = \begin{pmatrix} \hat{H}_D(\partial_x, \partial_y) + H_D(p_x, p_y) - E\hat{I} + 2\Gamma \begin{pmatrix} |A_0|^2 & 0 \\ 0 & |B_0|^2 \end{pmatrix} & \Gamma \begin{pmatrix} A_0^2 & 0 \\ 0 & B_0^2 \end{pmatrix} \\ -\Gamma \begin{pmatrix} A_0^{*2} & 0 \\ 0 & B_0^{*2} \end{pmatrix} & -\hat{H}_D^*(\partial_x, \partial_y) - H_D^*(p_x, p_y) + E\hat{I} - 2\Gamma \begin{pmatrix} |A_0|^2 & 0 \\ 0 & |B_0|^2 \end{pmatrix} \end{pmatrix}, \tag{S39}$$

where

$$H_D(p_x, p_y) = \begin{pmatrix} J_2\left(p_x^2 + p_y^2\right) & -J_1\sqrt{2}\left(p_y + ip_x\right) \\ -J_1\sqrt{2}\left(p_y - ip_x\right) & -J_2\left(p_x^2 + p_y^2\right) \end{pmatrix}, \tag{S40}$$

$$\hat{H}_D(\partial_x, \partial_y) = \begin{pmatrix} \Delta - 4J_2 - J_2\left(\partial_x^2 + \partial_y^2\right) & J_1\sqrt{2}\left(i\partial_y - \partial_x\right) \\ J_1\sqrt{2}\left(i\partial_y + \partial_x\right) & -\Delta + 4J_2 J_2\left(\partial_x^2 + \partial_y^2\right) \end{pmatrix}. \tag{S41}$$

To study modulational instability, we take $[\delta a; \delta a^*; \delta b; \delta b^*] = [\bar{C}_1; \bar{C}_2; \bar{C}_3; \bar{C}_4]e^{-i\lambda t + i\kappa_x x + i\kappa_y y} = \bar{\boldsymbol{C}}e^{-i\lambda t + i\kappa_x x + i\kappa_y y}$ and set $\kappa_x = 0$ to simplify further considerations. Eq. (S38) leads to the system of equations for amplitudes $\bar{\boldsymbol{C}}$: $\left(\hat{L} - \lambda\hat{I}\right)\bar{\boldsymbol{C}} = 0$. The positive imaginary part of λ, found from $\det\left(\hat{L} - \lambda\hat{I}\right) = 0$, indicates instability.

For the cross point at $p_x = p_y = 0$, existing at the intensities $\Gamma I_0 > \pm 2\left(\Delta - 4J_2\right)$ at the energy $E^{(0)} = \frac{\Gamma I_0}{2}$, with the amplitudes $|A_0|^2 = \dfrac{I_0}{2} - \dfrac{\Delta - 4J_2}{\Gamma}$, $|B_0|^2 = \dfrac{I_0}{2} + \dfrac{\Delta - 4J_2}{\Gamma}$, we find the energy detuning λ along the straight lines $I_0\Gamma + C = -2(\Delta - 4J_2)$ in the parameter plane (Γ, Δ):

$$\lambda = \pm\sqrt{\pm\frac{\sqrt{e^{-2i\varphi}\kappa_y^2\left(C^2\left(-1 + e^{2i\varphi}\right)^2 J_1^2 + 2C\left(-1 + e^{2i\varphi}\right)^2 \Gamma I_0 J_1^2\right) + 2\Gamma^2 I_0^2 J_2^2 \kappa_y^4}}{\sqrt{2}} + CJ_2\kappa_y^2 + \Gamma I_0 J_2\kappa_y^2 + 2J_1^2\kappa_y^2 + J_2^2\kappa_y^4}. \tag{S42}$$

We analyse Eq. (S42) for $C = 0$ at the line $I_0\Gamma = -2(\Delta - 4J_2)$, which is the negatively inclined existence boundary of the cross solution:

$$\lambda_{1,2} = \pm\sqrt{J_2^2\kappa_y^4 + 2\kappa_y^2 J_1^2}, \tag{S43}$$

$$\lambda_{3,4} = \pm\sqrt{-4(\Delta - 4J_2)J_2\kappa_y^2 + J_2^2\kappa_y^4 + 2J_1^2\kappa_y^2}. \tag{S44}$$

The imaginary part $\mathrm{Im}(\lambda_{1,2})$ is zero for all values of the wave number κ_y, therefore, $\lambda_{1,2}$ do not show any instability. The area of the stability can be determined from $\lambda_{3,4}$: it is a purely real quantity for $\Gamma > -\dfrac{J_1^2}{I_0 J_2}$ or equivalently $2J_1^2 \geq 4\left(\Delta - 4J_2\right)J_2$. In the nontrivial case, since $J_2\left(\Delta - 4J_2\right) < 0$, we conclude that $2J_1^2 \geq 4\left(\Delta - 4J_2\right)J_2$ for any J_2, Δ. Therefore, the cross point is stable. But in the trivial case, the area of parameters J_2, J_1 exists, for which $\mathrm{Im}(\lambda_{3,4}) > 0$, and the cross point becomes unstable. The boundary value of the detuning in the trivial phase is

$$\Delta_c = 4J_2 + \frac{J_1^2}{2J_2}. \tag{S45}$$

Note, for the given intensity, $-\Gamma I_0/2 = \Delta - 4J_2$, the upper branch and the point of the cross are degenerate. Hence, the line of stability $I_0\Gamma = -2(\Delta - 4J_2)$ appears in Fig. 1 in the main text for the upper branch at $\Delta < \Delta_c$. For

$\Delta > \Delta_c$, we analytically obtain the maximum growth rate $\max_{\kappa_y} \mathrm{Im}[\lambda_{3,4}]$ achieved at the wavenumber $\kappa_y^{\max}$:

$$\max_{\kappa_y} \mathrm{Im}[\lambda_{3,4}] = \frac{|J_1^2 + \Gamma I_0 J_2|}{|J_2|}; \tag{S46}$$

$$\kappa_y^{\max} = \pm\sqrt{\frac{|\Gamma I_0 J_2 + J_1^2|}{J_2^2}}. \tag{S47}$$

Equation (S42) at the other boundary of the existence of the cross solution (with $C = -2\Gamma I_0$) takes the form:

$$\lambda_{1,2,3,4} = \pm\sqrt{\pm\kappa_y^2 \Gamma I_0 J_2 - \Gamma I_0 J_2 \kappa_y^2 + 2J_1^2\kappa_y^2 + J_2^2\kappa_y^4}, \tag{S48}$$

from which we obtain the area of stability $\Gamma < \dfrac{J_1^2}{I_0 J_2}$.

Let us consider Eq. (S42) for the case $\varphi = \pi n, n \in \mathbb{Z}$:

$$\lambda_{1,2} = \pm\sqrt{J_2^2\kappa_y^4 + CJ_2\kappa_y^2 + 2J_1^2\kappa_y^2}, \tag{S49}$$

$$\lambda_{3,4} = \pm\sqrt{J_2^2\kappa_y^4 + CJ_2\kappa_y^2 + 2J_2\Gamma I_0\kappa_y^2 + 2J_1^2\kappa_y^2}. \tag{S50}$$

The boundaries of the cross stability are located on lines with $C = -\dfrac{2J_1^2}{J_2} - 2\Gamma I_0$ and $C = -\dfrac{2J_1^2}{J_2}$. These are the straight lines $I_0\Gamma = \pm 2(\Delta - 4J_2 - \frac{J_1^2}{J_2})$.

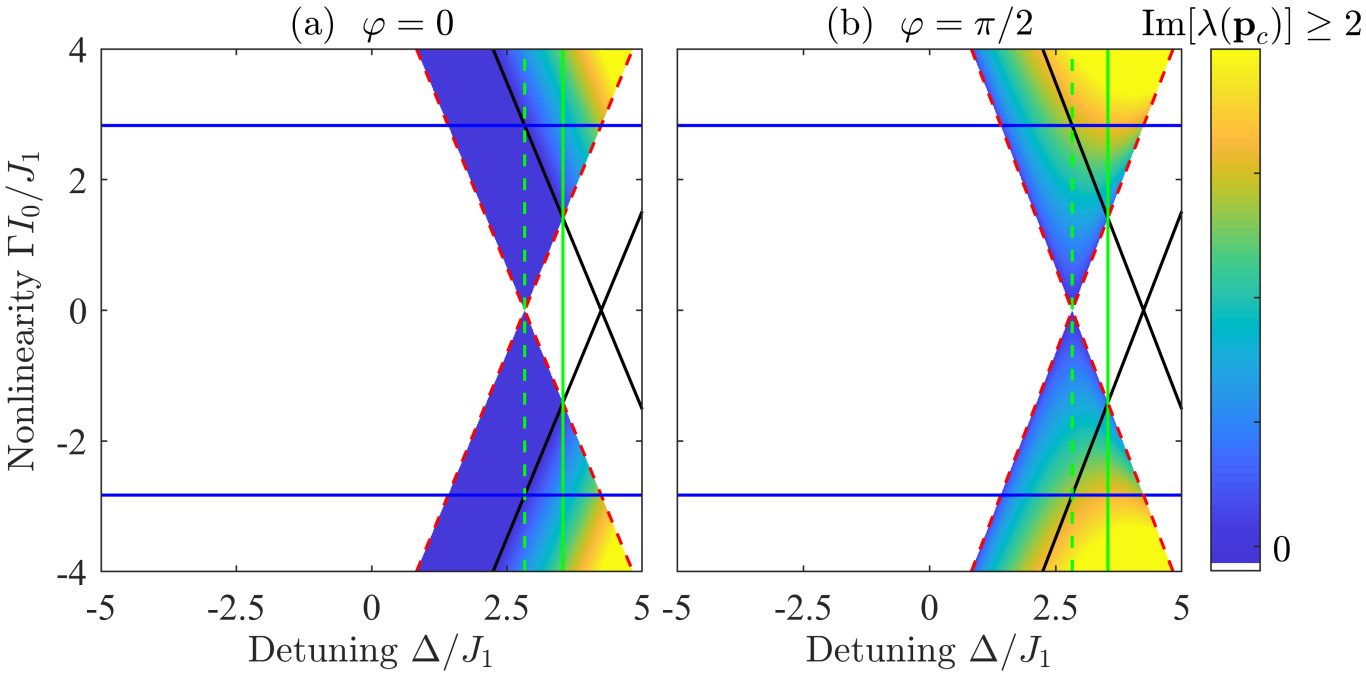

Figure S3: The maximum increment value $\max_\lambda[\mathrm{Im}(\lambda)]$ color-coded in the plane of parameters Δ/J_1, $\Gamma I_0/J_1$ for the cross point $E = \Gamma I_0/2$ at $p = 0$. Parameters are $J_2 = J_1/\sqrt{2}$, (a) $\varphi = 0$, (b) $\varphi = \pi/2$. Red dashed lines $\Gamma = \pm 2\left(4J_2 - \Delta\right)/I_0$ highlight the boundaries of the existence of the cross solution. On these lines, the cross point is stable in the nontrivial domain, $|\Delta| < 2\sqrt{2}$, whose upper boundary is marked with the green dashed line. In the trivial domain, the cross point is unstable at detunings larger $\Delta = J_1^2/2J_2 + 4J_2$ marked with a solid green line. The boundaries of the cross point stability for $\varphi = 0$ are black straight lines $I_0\Gamma = \pm 2(\Delta - 4J_2 - J_1^2/J_2)$. At $\varphi = 0$, the intersection point of the black lines with the boundary of the trivial phase at $\Gamma = \pm 2J_1^2/(J_2 I_0)$ (straight blue lines) defines the intensity, for which, by changing Δ, we can distinguish the trivial phase from the nontrivial one by observing a transition from stability to instability.

The color maps of the maximum increment value $\max_\lambda[\mathrm{Im}(\lambda)]$ in the parameter space for the cross solution $E = \Gamma I_0/2$ are plotted in Fig. S3 by using Eq. (S42). On our notations, linear stability of perturbation in y direction depends on the spinor phase angle φ. Making a generalization about this feature, we note that stability is conditional on the

mutual orientation $\Delta\theta = \theta_p - \theta_0$ of the symmetry-broken solution with $\boldsymbol{p}_0$ and perturbation with $\boldsymbol{p}_p$. In the nontrivial phase, it remains stable at $\Delta\theta = 0$ ($\varphi = 0$, $\theta_p = \pi/2$, $\theta_0 = \pi/2$) and exhibits the maximum transverse modulational instability at $\Delta\theta = \pi/2$ ($\varphi = \pi/2$, $\theta_p = \pi/2$, $\theta_0 = 0$).

Next, we describe modulational instability of the the background state $p_x = p_y = 0$ with a uniform intensity $\Gamma I_0 < \pm 2\,(\Delta - 4J_2)$. For definiteness, we consider the nonlinear mode from the band with energy $E = (\Delta - 4J_2) + \Gamma I_0$, and spinor components $B^{(0)} = 0$, $|A^{(0)}|^2 = I_0$ [see Eq. (S21)]. The solutions of equation $\det\left(\hat{L} - \lambda\hat{I}\right) = 0$ along the lines $I_0\Gamma + C = -2(\Delta - 4J_2)$ recast as

$$\lambda_{1,2} = \pm\sqrt{-F + D}\,, \tag{S51}$$

$$\lambda_{3,4} = \pm\sqrt{F + D}\,, \tag{S52}$$

being expressed through the auxiliary functions

$$F = \sqrt{C^4/4 + (C + \Gamma I_0)^2 J_2^2 \kappa_y^4 + \kappa_y^2(-J_2 C^2(C + \Gamma I_0) + 4J_1 C\Gamma I_0 + 2C^2 J_1^2)}\,, \tag{S53}$$

$$D = J_2^2\kappa_y^4 + \kappa_y^2(J_2 I_0\Gamma + 2J_1^2 - CJ_2) + C^2/2. \tag{S54}$$

At $C = 0$ we recover (S43) and (S44) for the cusp bifurcation point. Varying parameter C, one can reproduce the numerically-obtained map of instability shown in Fig. 1(c) of the main text. In the linear limit $\Gamma I_0 \to 0$, we obtain the spectrum

$$\lambda = \pm\left[-m_{\text{eff}} \pm \sqrt{(m_{\text{eff}} + J_2\kappa_y^2)^2 + 2J_1^2\kappa_y^2}\right]\,, \tag{S55}$$

where $m_{\text{eff}} = \Delta - 4J_2$. Assuming $|\lambda| \sim I_0 \sim \kappa_y^2 \sim \mu \ll 1$, where μ is the smallness parameter, from the determinant calculated to quadratic accuracy $\sim \mu^2$, we get

$$\lambda^2 = \left(\Gamma I_0 + J_2\kappa_y^2 + \frac{J_1^2\kappa_y^2}{m_{\text{eff}}}\right)^2 - \Gamma^2 I_0^2 = \kappa_y^2\left(J_2 + \frac{J_1^2}{m_{\text{eff}}}\right)\left[2\Gamma I_0 + \left(J_2 + \frac{J_1^2}{m_{\text{eff}}}\right)\kappa_y^2\right]\,. \tag{S56}$$

In the trivial phase $m_{\text{eff}} > 0$, similar to the nonlinear Schrödinger equation, instability only occurs for the self-focusing nonlinearity ($\Gamma < 0$), and the maximum increment of instability is achieved at $\kappa_y^2 = -\Gamma I_0/\left(J_2 + J_1^2/m_{\text{eff}}\right)$ with purely imaginary $\lambda = \pm i|\Gamma|I_0$. On the other hand, in the nontrivial phase $m_{\text{eff}} < 0$, for a fixed Γ the state can either be stable or unstable, depending on $|m_{\text{eff}}|$.

Figs. S4 and S5 illustrate dispersion and polarization of perturbation modes as a function of κ_y in the trivial and nontrivial phases in the weakly nonlinear regime. We characterize the perturbation modes' polarization by computing their time-averaged overlap with the linear Bloch waves $|\,\langle\delta\psi|\psi^{(0)}\rangle\,|^2$ and their sublattice imbalance $s_z = |\delta a|^2 - |\delta b|^2 = \langle\sigma_z\rangle$. In the trivial phase the perturbation modes maintain a moderate to large overlap with the linear Bloch waves, and $|s_z|$ remains large, indicating the perturbation modes are preferentially localized to a single sublattice. On the other hand, in the nontrivial phase $|s_z|$ rotates to the opposite pole of the Bloch sphere at large κ_y, reducing the effective strength of the nonlinearity-induced wave mixing.

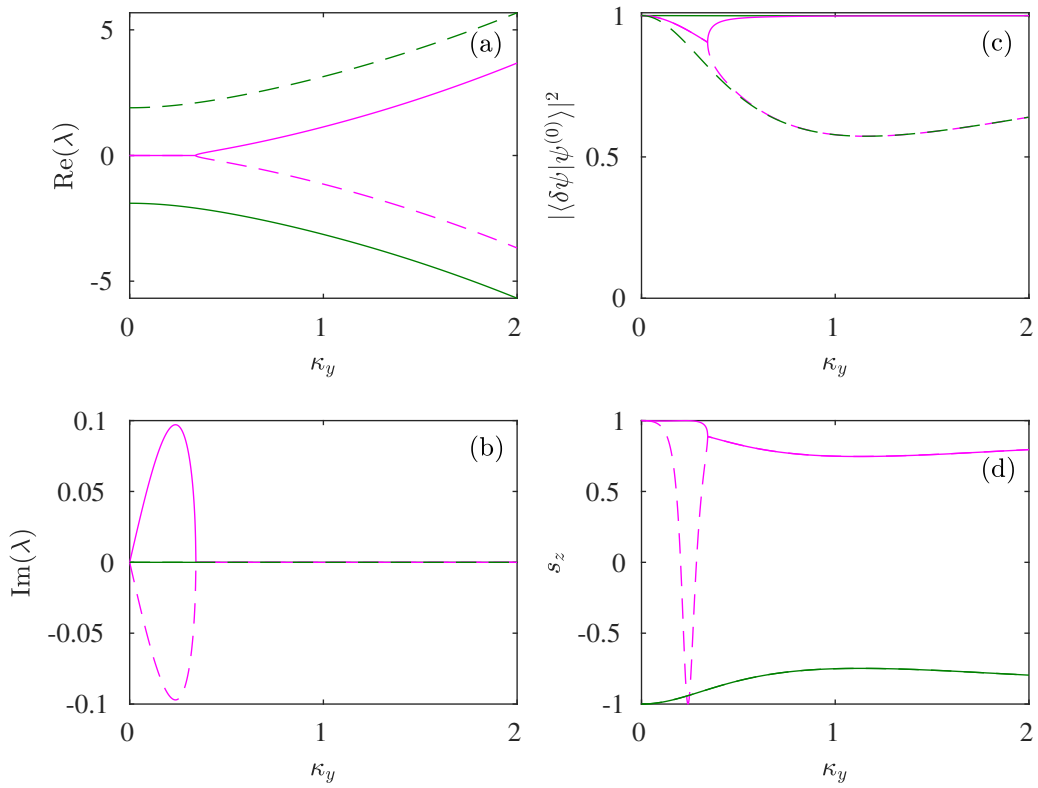

Figure S4: (a) Real and (b) imaginary parts of linear perturbation eigenvalues λ, (c) squared magnitude of the overlap between the perturbation modes and linear Bloch waves, (d) spin s_z projection of perturbation eigenvectors for the modulational instability in the weakly nonlinear regime, focusing nonlinearity $\Gamma = -1$, $I_0 = 0.1$, $m_{\text{eff}} = 1$ (trivial).

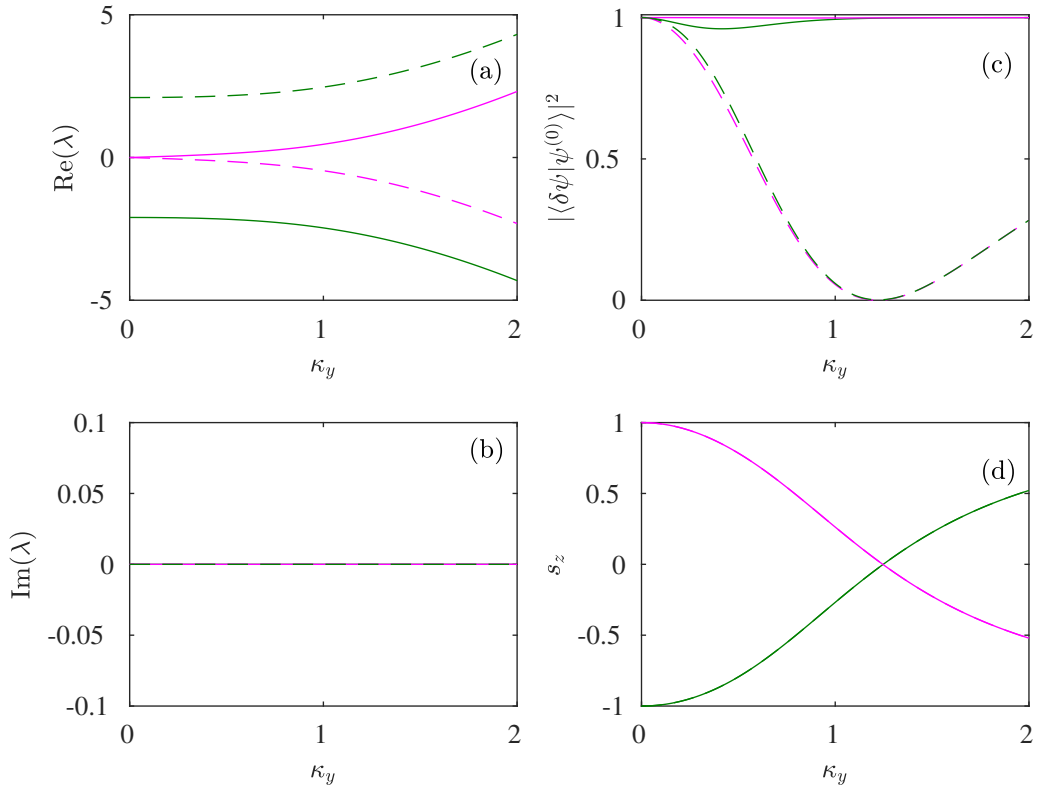

Figure S5: (a) Real and (b) imaginary parts of linear perturbation eigenvalues λ, (c) squared magnitude of the overlap between the perturbation modes and linear Bloch waves, (d) spin s_z projection of perturbation eigenvectors in the weakly nonlinear regime, focusing nonlinearity $\Gamma = -1$, $I_0 = 0.1$, $m_{\text{eff}} = -1$ (nontrivial).

4 Modulational instability dynamics and soliton formation

In this section we present additional details of the modulational instability dynamics summarised in Fig. 3 of the main text. We further characterize the dynamics by providing snapshots of the field intensity profiles in real and Fourier space at various times, as well as computing the linear and nonlinear parts of the conserved total energy $H = H_L + H_{NL}$,

$$H_L(t) = \int d\boldsymbol{k}\, \langle \psi(\boldsymbol{k},t)|\hat{H}_L(\boldsymbol{k})|\psi(\boldsymbol{k},t)\rangle\,, \quad H_{NL}(t) = \int d\boldsymbol{r}\, \langle \psi(\boldsymbol{r},t)|\hat{H}_{NL}(\boldsymbol{r})|\psi(\boldsymbol{r},t)\rangle\,. \tag{S57}$$

H_L provides a measure of which linear modes are excited by the wave field, while H_{NL} is sensitive to the field's localization.

Fig. S6 illustrates the dynamics of a perturbed nonlinear Bloch wave in the focusing instability regime ($\Delta = 0$, $\Gamma = -1.25$). For this choice of Δ the nonlinear Bloch wave lies at the lower edge of the lower band. At short times there is a clear amplification of the linearly unstable perturbation modes, which have wavevectors close to $\boldsymbol{k}_0$. As the instability continues to develop, a significant amount of energy is transferred to other wavevectors throughout the entire Brillouin zone, resulting in an increase of H_L. At the same time, strongly-localized soliton-like structures develop in real space, increasing $|\hat{H}_{NL}|$, as required for conservation of H. Thus, under the focusing nonlinearity the entire band becomes excited.

Next, we show in Fig. S7 the dynamics in the defocusing instability regime ($\Delta = 0$, $\Gamma = 2.5$). For short times we see a similar amplification of wavevectors close to $\boldsymbol{k}_0$. At longer times, there is a significant transfer of energy throughout the entire Brillouin zone, increasing H_L. However, in this case the dynamics decrease $|H_{NL}|$, indicating the field delocalizes in real space, distributing energy between both of the sublattices, and does not form any soliton-like structures. Interestingly, despite the qualitative differences between the real space field distribution in the focusing and defocusing cases, both exhibit a spreading of energy in Fourier space throughout the entire lower band, generating a large purity gap and allowing measurement of the band's Chern number.

Finally, Fig. S8 shows the dynamics in the oscillatory instability regime ($\Delta = 2$, $\Gamma = 2.5$). Again, at short times there is an amplification of wavevectors close to $\boldsymbol{k}_0$, before the entire Brillouin zone becomes populated at long times. For this Δ the initial Bloch wave lies at the upper edge of the lower band. Thus, the initial increase in H_L indicates a significant transfer of energy to the upper band. As the instability progresses, however, the spreading of energy within the lower band begins to dominate, leading to a decrease of H_L. In this case neither H_L nor H_{NL} converge to a stationary value and no stationary soliton-like structures are visible in the real space intensity profile.

As a further check, we also quantified the strength of interband mixing by calculating the time-dependent population of the upper band, $\int d\boldsymbol{k} |\langle u_+(\boldsymbol{k})|\psi(\boldsymbol{k},t)\rangle|^2$, with results shown in Fig. S9. In the focusing and defocusing instability examples, the interband mixing is negligible ($\approx 1\%$ of the total field energy), whereas in the case of oscillatory instability there is a significant transfer of energy into the upper band, which persists for long times. This strong energy transfer occurs due to the nonlinearity-induced band inversion, which enables resonant inter-band wave mixing.

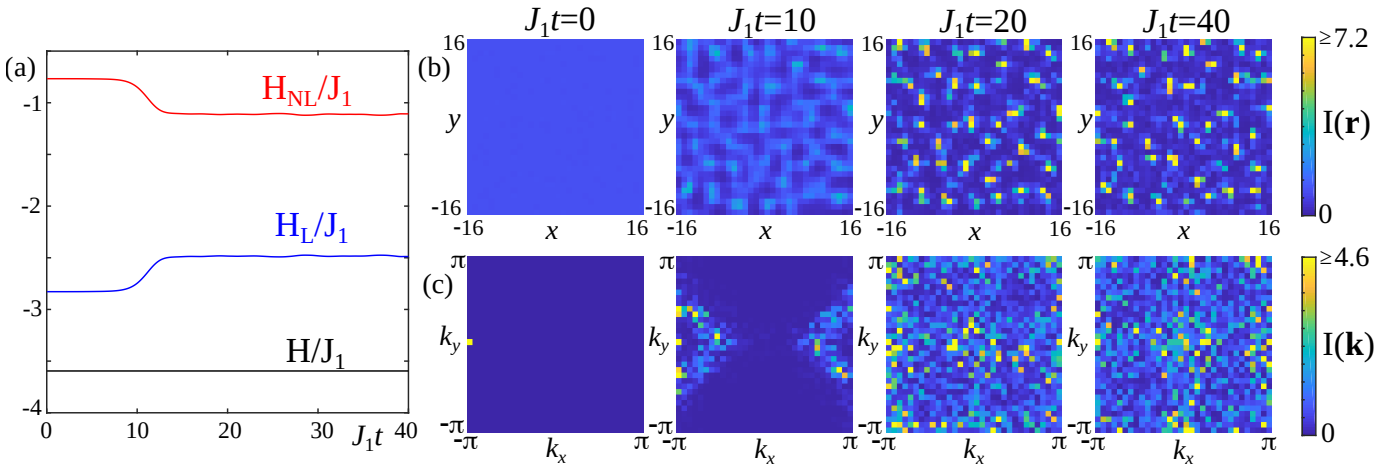

Figure S6: Dynamics of the modulational instability in the focusing regime, $\Delta = 0, \Gamma = -1.25$. (a) Time evolution of the linear H_L, nonlinear H_{NL}, and total $H = H_L + H_{NL}$ energies of the weakly-perturbed nonlinear Bloch wave. (b) Snapshots of the real space intensity $I(\boldsymbol{r}) = |\psi_a(\boldsymbol{r})|^2 + |\psi_b(\boldsymbol{r})|^2$ at different propagation times. (c) Snapshots of the Fourier space intensity $I(\boldsymbol{k}) = |\psi_a(\boldsymbol{k})|^2 + |\psi_b(\boldsymbol{k})|^2$ at different propagation times. In (b,c) the maximum of the colour scale is chosen to be 50% of the peak intensity at $J_1 t = 40$ in order to enhance the visibility of the field at the shorter times. Other parameters are the same as in Fig. 3 of the main text.

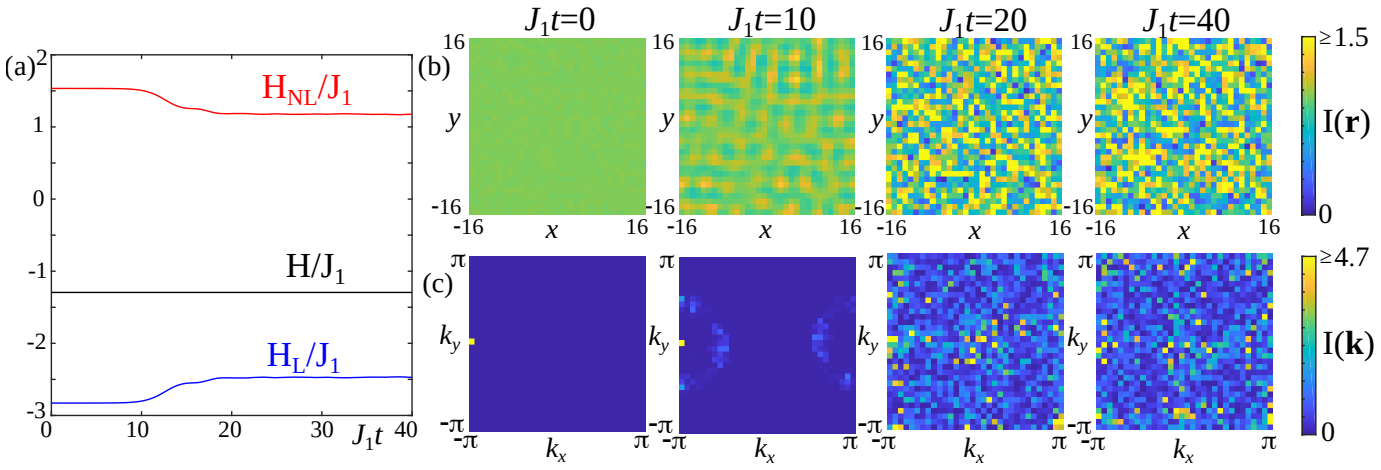

Figure S7: Dynamics of the modulational instability in the defocusing regime, $\Delta = 0, \Gamma = 2.5$. (a) Time evolution of the linear H_L, nonlinear H_{NL}, and total $H = H_L + H_{NL}$ energies of the weakly-perturbed nonlinear Bloch wave. (b) Snapshots of the real space intensity $I(\boldsymbol{r}) = |\psi_a(\boldsymbol{r})|^2 + |\psi_b(\boldsymbol{r})|^2$ at different propagation times. (c) Snapshots of the Fourier space intensity $I(\boldsymbol{k}) = |\psi_a(\boldsymbol{k})|^2 + |\psi_b(\boldsymbol{k})|^2$ at different propagation times. In (b,c) the maximum of the colour scale is chosen to be 50% of the peak intensity at $J_1 t = 40$ in order to enhance the visibility of the field at the shorter times. Other parameters are the same as in Fig. 3 of the main text.

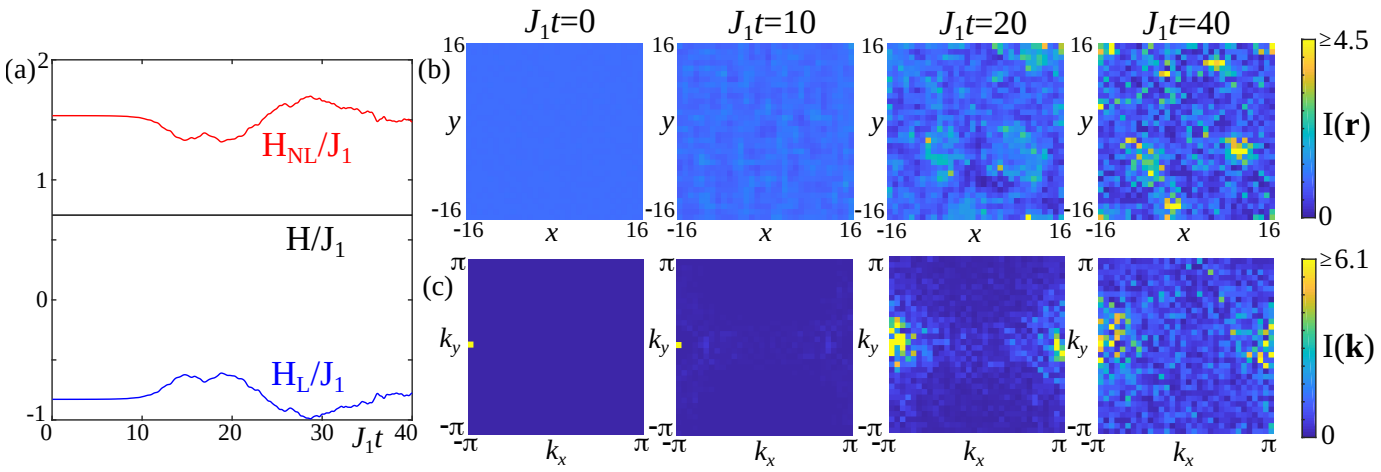

Figure S8: Dynamics of the modulational instability in the oscillatory instability regime, $\Delta = 2, \Gamma = 2.5$. (a) Time evolution of the linear H_L, nonlinear H_{NL}, and total $H = H_L + H_{NL}$ energies of the weakly-perturbed nonlinear Bloch wave. (b) Snapshots of the real space intensity $I(\boldsymbol{r}) = |\psi_a(\boldsymbol{r})|^2 + |\psi_b(\boldsymbol{r})|^2$ at different propagation times. (c) Snapshots of the Fourier space intensity $I(\boldsymbol{k}) = |\psi_a(\boldsymbol{k})|^2 + |\psi_b(\boldsymbol{k})|^2$ at different propagation times. In (b,c) the maximum of the colour scale is chosen to be 50% of the peak intensity at $J_1t = 40$ in order to enhance the visibility of the field at the shorter times. Other parameters are the same as in Fig. 3 of the main text.

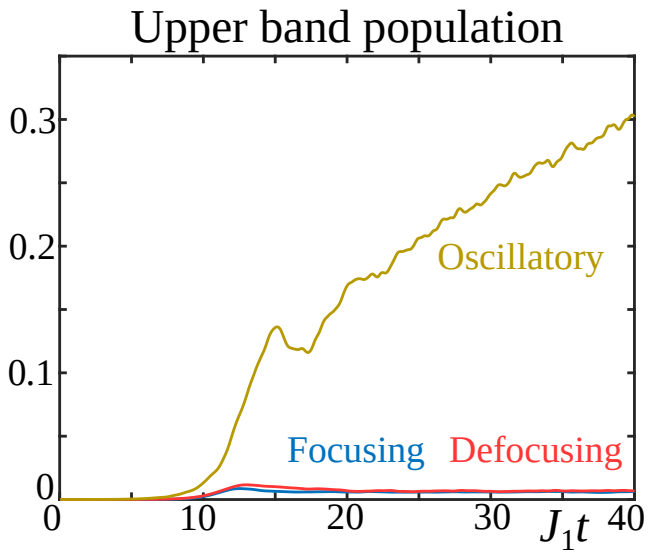

Figure S9: Dynamics of the upper band populations $\int d\boldsymbol{k} |\langle u_+(\boldsymbol{k})|\psi(\boldsymbol{k},t)\rangle|^2$ in the three regimes shown in Fig. 3 of the main text.

References

[S1] M. Z. Hasan and C. L. Kane, *Colloquium: Topological insulators*, Rev. Mod. Phys. **82**, 3045 (2010).

[S2] D. Xiao, M.-C. Chang, and Q. Niu, *Berry phase effects on electronic properties*, Rev. Mod. Phys. **82**, 1959 (2010).

[S3] T. Fösel, V. Peano, and F. Marquardt, *L lines, C points and Chern numbers: understanding band structure topology using polarization fields*, New J. Phys. **19**, 115013 (2017).